Logical quantum circuits protected by the Steane code for specific noises in trapped ions

Sheng-Chen Liu[⑩],[1] Lin Cheng,[1,3] Liang-You Peng[⑩],[1,2,3,*] and Qihuang Gong[1,2,3]

[1]*State Key Laboratory for Mesoscopic Physics and Frontiers Science Center for Nano-optoelectronics, School of Physics, Peking University, Beijing 100871, China*

[2]*Collaborative Innovation Center of Extreme Optics, Shanxi University, Taiyuan 030006, China*

[3]*Beijing Academy of Quantum Information Sciences, Beijing 100193, China*

In the presence of physical noise of all platforms for quantum computation, quantum error correction (QEC) becomes a critical way to realize quantum algorithms with large quantum volumes. In order to understand the influence of quantum noise on QEC codes and further improve the performance of logical circuits, the noises should be accurately analyzed with proper models. Here we focus on the trapped-ion system. Fundamentally, we start from the laser pulses of the quantum gates in the circuits and extract the noise components from the complete evolution of the quantum states, beyond the standard depolarizing model and other simplified models. Our simulations indicate that the logical performance under real noises is significantly better than that predicted by previous models. Meanwhile, the advantage of QEC is shown in the levels of one, two, and more logical qubits. Moreover, we can increase the logical fidelity by the method of ion mapping, which is based on knowledge of the specific noise distribution of different ions. Some powerful evidence from the numerical results demonstrates the possibility to access fault-tolerant quantum computation with the trapped-ion system.

I. INTRODUCTION

As the scale of quantum computation becomes larger, the noise of physical systems attacks the quantum information more severely. For future quantum computers, which can solve some real problems better than classical computers, the scheme of quantum error correction (QEC) [1,2] is now believed to be an indispensable ingredient. In the framework of QEC, qubits are redundantly encoded in a larger Hilbert space, where the local errors can be recognized and corrected. With physical error rates lower than some threshold, which is called the break-even point, reliable logical results can be obtained if the QEC process is elaborately designed in a fault-tolerant (FT) way.

During the last three decades, many types of QEC codes have been developed, while several cases have been demonstrated in different physical platforms. The surface code [3] has generally been considered as the best candidate for a superconducting system because the two-dimensional lattice structure of the surface code matches the distribution of qubits. In current experiments, one logical qubit has reached the break-even point [4] and the performance can be better with a larger code [5]. Recently, neutral atom arrays can operate many logical qubits of color codes [6], showing huge potential for scalability. Meanwhile, for the trapped-ion system, which has the advantage of all-to-all connectivity, it is very convenient to realize the operations between different logical codes and then the repetitive QEC cycles [7–9].

In this work, we focus on the trapped-ion system. To realize complete QEC, the different sections, including logical qubits encoding, syndrome extraction, logical operation, and final measurements, should be fault-tolerant, which means that the physical errors at any position cannot spread in a dangerous way. Each module suitable for trapped-ion systems has been discussed in detail in previous works [10–13], where Mølmer-Sørensen (MS) gates [14–16] are applied for two-qubit operations. However, the physical noises in the system are usually considered as depolarizing channels or other models based on some phenomenological parameters. In fact, the noises in real devices for quantum computation may be highly biased, resulting in different performance of QEC and some space for further optimization [17–19]. The issue also needs careful treatment in the trapped-ion platform.

In this work, we attempt to accurately analyze the noises from the fundamental evolution of MS gates, which contribute most to the errors in quantum circuits. With several methods of noise decomposition [20–22], we can use several Clifford channels to describe the noisy MS gates;

then the Clifford channels can be efficiently simulated in classical computers [23]. The subsequent results will be presented for the performance of different logical circuits, which are closer to reality. Since the laser pulses and fidelities for MS gates which entangle different ion pairs are not identical, it is possible to further improve the logical results by arranging the more dangerous qubits in the circuits with the ions that are less sensitive to physical errors. Our simulations are not restricted to one logical qubit, but are also suitable for more complicated logical circuits with many logical qubits, providing more evidence for the effectiveness of QEC in future quantum computation.

The organization of this paper is as follows. In Sec. II, we briefly review the QEC protocol based on the Steane code [24] for one logical qubit in the trapped-ion system. In order to establish the error models, we begin the analysis from the pulse scheme of MS gates in Sec. III, and extract the noise components from the complete evolution of the quantum states. In Sec. IV, we extend our simulations to more logical qubits with some specific circuits. All numerical results are presented and analyzed in Sec. V. Finally, we conclude our results and discuss the outlook in Sec. VI.

II. QEC BASED ON TRAPPED-ION SYSTEM

In order to demonstrate the influence of realistic trapped-ion noise on QEC, first we need to choose a proper code to define the logical qubits. Compared with the surface code, which is generally considered as the best candidate for a superconducting system due to the compatibility of the two-dimensional lattice architecture [4], the seven-bit Steane code [24] is a smaller one which can be conveniently realized in trapped-ion devices [8,13]. Moreover, the Steane code can support convenient logical operations, which will be discussed in the following.

A. Basic properties of the Steane code

The Steane code constructs one logical qubit with seven physical qubits, while two ancillary qubits can extract error information with an FT scheme [25]. Mathematically, logical states without errors are those simultaneous eigenvectors with $+1$ eigenvalue of six commuting stabilizers,

$$S_x^{(p)} = \prod_{i \in I_p} X_i, \quad S_z^{(p)} = \prod_{i \in I_p} Z_i, \quad p \in \{1, 2, 3\}, \quad (1)$$

where the physical qubit number i of the corresponding Pauli operators X_i and Z_i is taken from the set I_p for the pth X-type or Z-type stabilizer [see Fig. 1(a)]. Because of the fact that the stabilizers in Eq. (1) contain only X or Z operators, phase- and bit-flip errors on any qubit can be identified by $S_x^{(p)}$ and $S_z^{(p)}$ separately. Specifically, if the phase-flip error occurs on one qubit, the parity of $S_x^{(p)}$ on

the plaquettes adjacent to this qubit will change to -1. The same is true with bit-flip errors and $S_z^{(p)}$.

For logical Pauli operators, they can be realized as $X_L = \prod_i X_i$ and $Z_L = \prod_i Z_i$. Combining with the stabilizers in Eq. (1), we can obtain simpler expressions as

$$X_{L,l} = \prod_{i \in I_{L,l}} X_i, \quad Z_{L,l} = \prod_{i \in I_{L,l}} Z_i, \quad l \in \{1, 2\}, \quad (2)$$

where l can be chosen arbitrarily for convenience. Each of these logical Pauli operators acts on an edge of the triangle which denotes the Steane code in Fig. 1(a). It is worth noting that these Pauli operators are not only used to evolve the quantum circuits, but also measured to extract information of the quantum states, while different versions
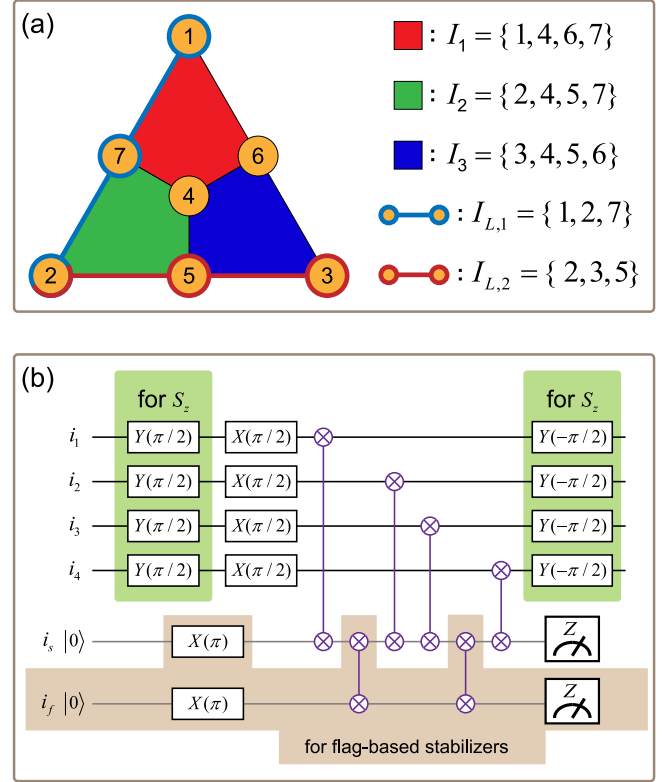

FIG. 1. A sketch of the Steane code. (a) Physical qubits with numbers are represented by yellow circles, while X-type and Z-type stabilizers are defined on three plaquettes with different colors. Besides, two weight-three logical operators act on the colored edges. (b) The circuits for nondemolition stabilizer readout can be drawn in a unified form. The upper four qubits correspond to the stabilizer to be measured and i_s denotes the ancillary qubit for readout. If the stabilizer is measured in an unflagged version, the content in the brown box including the flag qubit i_f can be omitted. The optional Y rotations in the green boxes are added for Z-type stabilizers and omitted for X-type stabilizers. For convenience, the numbers of ancillary qubits are set as $i_s = 8$ and $i_f = 9$.

of logical Pauli operators are suitable for different information in different parts of the circuits, which will be demonstrated in the following sections.

After clarifying the stabilizers and the simple Pauli operators which are closely related to the code space and the error syndrome, realizing other logical operations becomes the next crucial component of FT quantum computation. For those operations in the group of Clifford gates, the Steane code permits a transversal realization [26], which is a low-cost way in experiments. In Sec. IV, we will present the applications of Clifford gates in several logical quantum circuits.

B. Trapped-ion-based quantum gates

Quantum circuits can always be decomposed into a series of gates on physical qubits. Here, we will introduce the physical gates in the trapped-ion system. In our calculation, we choose two hyperfine sublevels of one $^{171}\text{Yb}^+$ ion as a qubit, which can be coherently manipulated by Raman lasers with wavelength $\lambda = 355$ nm [27,28]. With the help of ancillary states, the initialization and measurement processes are accessible in experiments [29]. Moreover, an arbitrary single-qubit rotation in the Bloch sphere can be realized by changing several laser parameters, e.g., Rabi frequency Ω, phase ϕ, detuning μ, and pulse duration τ [29]. In particular, we focus on those rotations with X, Y, Z axes on the Bloch sphere. These operations are denoted as

$$P_i(\theta) = e^{-i(\theta/2)P_i}, \quad P \in \{X, Y, Z\}, \tag{3}$$

where θ is the rotation angle. For two-qubit operations, controlled NOT (CNOT) gates are usually applied in many quantum circuits to generate entanglement. However, in the trapped-ion hardware, the MS scheme is the common way to realize this function by [14,30]

$$XX_{i_1 i_2}(\theta) = e^{-i(\theta/2)X_{i_1}X_{i_2}}. \tag{4}$$

In fact, the MS gate is connected with the CNOT gate by several single-qubit gates. In this work, we choose one of the consistent relations between them [31]:

$$\text{CNOT}_{i_1 i_2} = Y_{i_1}\left(-\frac{\pi}{2}\right) XX_{i_1 i_2}\left(-\frac{\pi}{2}\right) X_{i_1}\left(\frac{\pi}{2}\right)$$
$$\times X_{i_2}\left(\frac{\pi}{2}\right) Y_{i_1}\left(\frac{\pi}{2}\right). \tag{5}$$

We will substitute MS gates (i.e., $XX_{i_1 i_2}(-(\pi/2))$) for CNOT gates with Eq. (5) in the following.

C. Fault-tolerant protocol for QEC

In this section, we will review the protocol for the full round of QEC with the trapped-ion hardware, which has been discussed in several works [9,11]. Our complete QEC protocol for one logical qubit is schematically shown in Fig. 2. Even though the detailed error models have not been discussed, it is necessary to emphasize the fault tolerance of the protocol here, which means that any single-qubit error occurring on any location (including on the syndrome check) in the circuit can always be corrected.

Let us introduce different parts of the QEC protocol. When the logical quantum circuits start, the logical qubits need to be initialized to the code space, which is realized by the encoding circuit with a flag qubit, given in Appendix A.
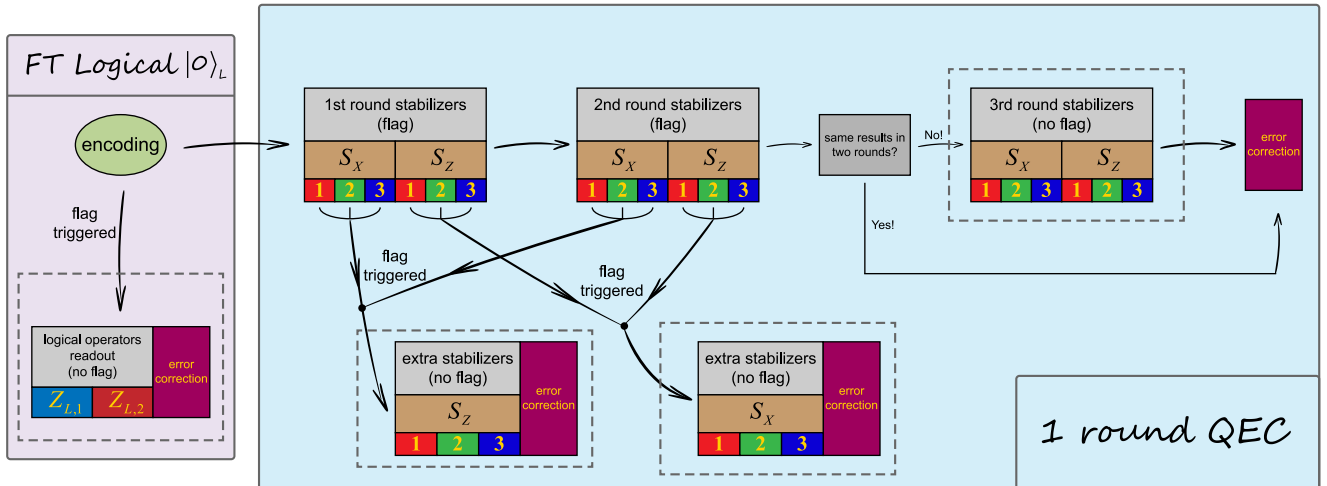

FIG. 2.   A schematic diagram of the QEC protocol. The light purple box for preparing the logical $|0\rangle_L$ includes the encoding circuit with the flag qubit and the subsequent correction module with readout of logical operators. The main body of the QEC process is presented in the light blue box. Each round of stabilizer readout is represented by a rectangle with some detailed components, where the smaller colored rectangles with numbers denote the circuit in Fig. 1(b) for the corresponding stabilizers. Any triggered flag will take the process to the branch of extra stabilizers.

No matter what logical state is required, first $|0\rangle_L$ is prepared, while subsequent rotations are used for other states. Once the flag is triggered (i.e., the measurement of the flag qubit yields -1), we turn to measure the weight-three logical operators $Z_{L,1}$ and $Z_{L,2}$ to extract the syndrome of possible correlated errors in the encoding circuit. According to the results of $Z_{L,1}$ and $Z_{L,2}$, some specific Pauli X gates could be added to correct some dangerous errors. Otherwise, the main body of QEC starts, with the frequent modules for the stabilizer readout in Fig. 1(b). Two rounds of measurements for the six stabilizers with a flag qubit are carried out serially. However, if any flag is triggered during the above process, the measurements for the stabilizers will stop immediately because of the implied correlated errors. Meanwhile, we are supposed to jump to the measurements for three stabilizers conjugate of the interrupted one without the flag qubit. The results of both the qubit for stabilizer readout and the flag qubit determine the possible errors, and the corresponding correction circuit can be constructed according the rules in Ref. [11]. If we finish the total of 12 measurements for the stabilizers successfully, the results in two rounds will be compared. The same results will lead to the final error correction directly, while different results will bring about the third round of stabilizers readout.

III. NOISE ANALYSIS WITH TRAPPED IONS

Now that a full view of the QEC protocol has been obtained, we are more concerned about how the specific noises in the trapped-ion devices affect the performance of QEC. Among different parts of the qubit control, two-qubit gates are most noisy in experiments with trapped ions [28,32]. As a consequence, the fidelity of the logical qubit is mainly decided by these two-qubit gates. In several recent works, the authors have considered several customized trapped-ion noise models [10,11,33]. However, most of them are based on the depolarizing channel or the over-rotation error, which are still highly simplified from real noise. In this section, we begin with the segmented pulse which is the common scheme for MS gates in experiments [34,35] nowadays and analyze the important sources of noise with the tools for the decomposition of quantum channels [20,21,36,37]. Then the components of the noise can be transferred to the QEC circuits for subsequent simulations. With more specific noise models, we believe that a better approximated performance of the logical qubit can be obtained, while the infidelity of the logical qubit can also be further suppressed by some careful designs.

A. MS gates realized by segmented pulses

We consider a chain of N ions trapped in an external electric field with center-of-mass (COM) frequencies ω_z and ω_x, respectively, in the axial and radial directions. Under Raman beams with wave vector difference Δk along the x axis shining on two target ions marked as i_1 and i_2, the N radial motional modes in the x direction are driven to entangle the two ions [38]. After a duration τ of the interaction, the time evolution of the system becomes [15,39]

$$U_{\mathrm{MS}} = \exp\left[\sum_{i=i_1,i_2}\sum_k (\alpha_k^i a_k^\dagger - \alpha_k^{i*} a_k)X_i - i\frac{\theta}{2}X_{i_1}X_{i_2}\right]. \tag{6}$$

The first term describes the qubit-motion entanglement where a_k $(a_k^\dagger)$ is the annihilation (creation) operator of motional mode k and

$$\alpha_k^i = -i\eta_k b_k^i \int_0^\tau \Omega(t)\sin(\mu t)e^{i\omega_k t}\,dt \tag{7}$$

is the coupling strength, where $\eta_k = \Delta k\sqrt{\hbar/2M\omega_k}$ is the Lamb-Dicke parameter, b_k^i is the normalized amplitude of the ith ion and the kth mode with frequency ω_k, and M is the mass of a single ion. The second term is the qubit-qubit coupling with the coefficient of

$$\theta = -4\sum_k \eta_k^2 b_k^{i_1} b_k^{i_2} \int_0^\tau dt \int_0^t dt'\,\Omega(t)\Omega(t')$$
$$\times \sin[\omega_k(t-t')]\sin(\mu t)\sin(\mu t'). \tag{8}$$

In order to reach the goal of the MS gate in Eqs. (4) and (5), the qubits and the motional modes need to be disentangled, which can be written as

$$\alpha_k^i = 0, \quad \forall k, \tag{9}$$

while the qubit-qubit coupling is $\theta = -(\pi/2)$. Here we note that, for a given mode k, satisfying Eq. (9) does not depend on the ion number i. Technically, a set of parameters of the laser pulse, such as the amplitude, phase and detuning, are controlled to satisfy the above conditions [15,40,41]. In fact, we have already chosen the amplitude-modulated pulse in the time domain in Eqs. (7) and (8) for convenience, where the phase of the pulse is set to zero and the detuning is a constant during the whole interaction. Then the pulse is equally divided into $N_{\mathrm{seg}} > 2N + 1$ segments with tunable amplitudes to ensure the existence of solutions [42]. However, the experimental parameters fluctuate due to some noises. Thus the equalities are perturbed to some extent and residual qubit-motion entanglement is generated (i.e., $\alpha_k^i \neq 0$).

Consequently, the infidelity of MS gates emerges with the form

$$\delta F \approx \frac{4}{5}\sum_k \left(|\alpha_k^{i_1}|^2 + |\alpha_k^{i_2}|^2\right)(2\bar{n}_k + 1), \tag{10}$$

where the averaged stimulated phonon number $\bar{n}_k$ can be safely chosen as 0.5 under the current experimental conditions [43]. To be specific, the noises usually come from the

fluctuations of motional-mode frequencies, laser intensities, laser frequencies, and some other parameters [15,35], but we mainly discuss the motional-mode frequencies in this work due to their predominance in many experiments [40,44,45]. For other sources, the following analyses are also effective.

In order to reduce the influence of such noises, the stabilization conditions can be added by [44]

$$\frac{\partial \alpha_k^i}{\partial \omega_k} = 0, \quad \forall k. \tag{11}$$

Equations (9) and (11) can be solved linearly without intractable problems. Finally, we only need to scale the pulse amplitude to satisfy the qubit-qubit entangling strength in Eq. (8).

B. Noise models

This section is devoted to analyze the noises of MS gates more practically. We will first review the description of quantum channels and the conventional depolarizing noise. Then we propose our specific noise models under the fluctuations of experimental parameters. With these noise components, the performance of the logical qubits can be better simulated.

1. Basic quantum channels

In order to describe the influence of noise, it is necessary to introduce the density matrix ρ to represent the quantum state mixed by nonunitary evolutions. In this work, we do not consider the leakage of quantum information out of the $|0\rangle$, $|1\rangle$ space due to the usual predominance of the gate errors [9,13]. Therefore, any quantum operation with noise belongs to completely positive trace-preserving

maps, which can be written as

$$\mathcal{E}(\rho) = \sum_n p_n E_n \rho E_n^\dagger, \tag{12}$$

where the Kraus operators E_n with probability p_n satisfy the relation

$$\sum_n p_n E_n^\dagger E_n = I. \tag{13}$$

In the standard depolarizing error model for the two-qubit MS gates which is denoted by $\mathcal{E}_{\mathrm{MS}}^{\mathrm{dep}}$, the Kraus operators E_n for $1 \leq n \leq 15$ are selected from the Pauli operators $\{I, X, Y, Z\}^{\otimes 2} \setminus \{II\}$ with an equal probability of $p/15$. Meanwhile, the correct case $E_0 = II$ occurs with probability of $1 - p$. When the detailed information of the noise channel is unknown, this depolarizing model is adopted naturally [3,46]. Integrating over the two-qubit states with the uniform measure [47], we can obtain the infidelity connected to the phenomenological probability p as

$$\delta F^{\mathrm{dep}} = \frac{4}{5} p, \tag{14}$$

with the detailed derivation being presented in Appendix B.

2. Clifford decomposition

However, with knowledge of the above MS pulses, it is possible to analyze the noise channel more accurately. For an arbitrary initial two-qubit state

$$\rho_i = \begin{pmatrix} \rho_{00,00} & \rho_{00,01} & \rho_{00,10} & \rho_{00,11} \\ \rho_{01,00} & \rho_{01,01} & \rho_{01,10} & \rho_{01,11} \\ \rho_{10,00} & \rho_{10,01} & \rho_{10,10} & \rho_{10,11} \\ \rho_{11,00} & \rho_{11,01} & \rho_{11,10} & \rho_{11,11} \end{pmatrix} \tag{15}$$

in the basis of $|\pm\rangle^{\otimes 2}$ and the thermal motional state ρ_{th}, the MS gate will produce the final two-qubit state by tracing out the motional part after the gate evolution [15]:

$$\begin{aligned} \rho_f &= \mathrm{Tr}_m(U_{\mathrm{MS}} \rho_i \otimes \rho_{\mathrm{th}} U_{\mathrm{MS}}^\dagger) \\ &\approx \begin{pmatrix} \rho_{00,00} & (1-\varepsilon_{i_2})e^{-i\theta}\rho_{00,01} & (1-\varepsilon_{i_1})e^{-i\theta}\rho_{00,10} & (1-\varepsilon_+)\rho_{00,11} \\ (1-\varepsilon_{i_2})e^{i\theta}\rho_{01,00} & \rho_{01,01} & (1-\varepsilon_-)\rho_{01,10} & (1-\varepsilon_{i_1})e^{i\theta}\rho_{01,11} \\ (1-\varepsilon_{i_1})e^{i\theta}\rho_{10,00} & (1-\varepsilon_-)\rho_{10,01} & \rho_{10,10} & (1-\varepsilon_{i_2})e^{i\theta}\rho_{10,11} \\ (1-\varepsilon_+)\rho_{11,00} & (1-\varepsilon_{i_1})e^{-i\theta}\rho_{11,01} & (1-\varepsilon_{i_2})e^{-i\theta}\rho_{11,10} & \rho_{11,11} \end{pmatrix}. \end{aligned} \tag{16}$$

Here we have considered the first-order approximation, which is sufficient for our calculations. The parameters in Eq. (16) are connected with the qubit-motion entanglement as the form

$$\varepsilon_{i_\xi} = 2 \sum_k |\alpha_k^{i_\xi}|^2 (2\bar{n}_k + 1), \quad \xi \in \{1, 2\},$$

$$\varepsilon_\pm = 2 \sum_k |\alpha_k^{i_1} \pm \alpha_k^{i_2}|^2 (2\bar{n}_k + 1), \tag{17}$$

and the qubit-qubit entanglement is $\theta = -\pi/2$. Although the noise may disturb the value of θ, it will only contribute to the second-order term, which will be ignored hereafter.

In the superoperator representation where the d-dimensional density matrix is vectorized as $\boldsymbol{\rho}$ with d^2 elements, the quantum channel is a linear mapping, which can be represented by a d^2-dimensional matrix $\mathbf{S}$ [37]. After the quantum channel, the density matrix will change to

$$\boldsymbol{\rho}' = \mathbf{S}\boldsymbol{\rho}. \tag{18}$$

This means that the noisy quantum circuit can be directly simulated by a matrix multiplication [48], but the consumed computation resource will increase exponentially because of the dimension expansion by the tensor product. However, quantum channels can always be decomposed to Clifford channels and Pauli measurements [21]. With the decomposition, we can sample from the channels for each noisy gate in the whole circuit repeatedly and then simulate the whole circuit efficiently [49].

Before we discuss the above Clifford decomposition, it can be noticed that in Eq. (16) the noisy MS gate only multiplies each element of the density matrix by a number, without mixing different elements. This fact will result in a diagonal matrix of the superoperator. Based on this property, the quantum channel of the MS gate can be decomposed in a relatively simple way:

$$\rho_f = \mathcal{E}_{\mathrm{MS}}^{\mathrm{Clif}}\left(XX_{i_1 i_2}\left(-\frac{\pi}{2}\right)\rho_i XX_{i_1 i_2}^{\dagger}\left(-\frac{\pi}{2}\right)\right), \tag{19}$$

where the Kraus operators for $\mathcal{E}_{\mathrm{MS}}^{\mathrm{Clif}}$ are

$$E_n \in \left\{I_{i_1}I_{i_2}, X_{i_1}I_{i_2}, I_{i_1}X_{i_2}, X_{i_1}X_{i_2}, X_{i_1}\left(\frac{\pi}{2}\right)X_{i_2}\left(\frac{\pi}{2}\right),\right.$$
$$\left. X_{i_1}\left(-\frac{\pi}{2}\right)X_{i_2}\left(-\frac{\pi}{2}\right)\right\}, \tag{20}$$

and the corresponding probabilities are

$$p_{II} = 1 - \frac{\varepsilon_{i_1} + \varepsilon_{i_2} + \varepsilon_+}{4},$$
$$p_{XI} = \frac{\varepsilon_{i_1} - \varepsilon_{i_2} + \varepsilon_-}{4},$$
$$p_{IX} = \frac{-\varepsilon_{i_1} + \varepsilon_{i_2} + \varepsilon_-}{4}, \tag{21}$$
$$p_{XX} = \frac{\varepsilon_{i_1} + \varepsilon_{i_2} - \varepsilon_+}{4},$$
$$p_{X^+X^+} = p_{X^-X^-} = \frac{\varepsilon_+ - \varepsilon_-}{4}.$$

For brevity, the subscript has been denoted with $X^{\pm}$ for $X(\pm(\pi/2))$. One can refer to Appendix C for a detailed derivation.

In Eq. (19), the noisy MS gate acts on qubits i_1 and i_2 in two steps: first the ideal unitary XX evolution and then

the following noise channel $\mathcal{E}_{\mathrm{MS}}^{\mathrm{Clif}}$. If the noise decreases to zero, $\mathcal{E}_{\mathrm{MS}}^{\mathrm{Clif}}$ will tend to the identity operator, which can be seen in Eq. (21).

It is also worth noting that the decomposition probabilities in Eq. (21) may be negative. We can deal with the problem with the algorithm for quasiprobability distributions given in Ref. [21], but the noise strength must be restricted in the very low regime when the quantum volume becomes large.

3. Pauli twirling approximation

In order to maintain a moderate consumption of computation resource for more qubits and gates, it is necessary to approximate the noise channel with positive Kraus components. One convenient method is the Pauli twirling approximation (PTA), where only the Pauli channels are left in the decomposition [50,51]. Performance cannot be promised for the distance between the real channel and the approximated channel [36], but the errors can be cancelled out in the level of circuits [50]. We will check the effectiveness of the PTA in Sec. V for our circuits.

Extracting the diagonal elements of the χ matrix, we can obtain the Pauli twirling components of the quantum channel [50]. In the χ-matrix description in Pauli basis for two qubits, any quantum channel can be expressed as

$$\mathcal{E}(\rho) = \sum_{n,n'=0}^{15} \chi_{n,n'} E_n \rho E_{n'}^{\dagger}, \quad E_n, E_{n'} \in \{I, X, Y, Z\}^{\otimes 2}, \tag{22}$$

with the diagonal elements $\chi_{n,n} \geq 0$ [22]. The Pauli twirling removes all off-diagonal elements, leaving the channel approximated to

$$\mathcal{E}^{\mathrm{PTA}}(\rho) = \sum_{n=0}^{15} \chi_{n,n} E_n \rho E_n^{\dagger}, \quad E_n \in \{I, X, Y, Z\}^{\otimes 2}. \tag{23}$$

In Eq. (20), the non-Pauli components $X_{i_1}(\pm(\pi/2))X_{i_2}(\pm(\pi/2))$ contribute to off-diagonal elements in the χ matrix. After the Pauli twirling, they disperse to the other four Pauli components evenly, resulting in the updated probabilities:

$$p_{II}' = p_{II} + \frac{1}{4}(p_{X^+X^+} + p_{X^-X^-})$$
$$= 1 - \frac{2\varepsilon_{i_1} + 2\varepsilon_{i_2} + \varepsilon_+ + \varepsilon_-}{8} = 1 - \frac{\varepsilon_{i_1} + \varepsilon_{i_2}}{2},$$
$$p_{XI}' = p_{XI} + \frac{1}{4}(p_{X^+X^+} + p_{X^-X^-})$$
$$= \frac{2\varepsilon_{i_1} - 2\varepsilon_{i_2} + \varepsilon_+ + \varepsilon_-}{8} = \frac{\varepsilon_{i_1}}{2},$$

$$p'_{IX} = p_{IX} + \frac{1}{4}(p_{X+X+} + p_{X-X-})$$

$$= \frac{-2\varepsilon_{i_1} + 2\varepsilon_{i_2} + \varepsilon_+ + \varepsilon_-}{8} = \frac{\varepsilon_{i_2}}{2},$$

$$p'_{XX} = p_{XX} + \frac{1}{4}(p_{X+X+} + p_{X-X-})$$

$$= \frac{2\varepsilon_{i_1} + 2\varepsilon_{i_2} - \varepsilon_+ - \varepsilon_-}{8} = 0, \qquad (24)$$

where only the single-qubit errors are retained (see Appendix D for details). This will be convenient for our numerical analysis in the following sections. Similar to the Clifford decomposition channel $\mathcal{E}_{MS}^{Clif}$, the PTA channel for the MS gate is denoted by $\mathcal{E}_{MS}^{PTA}$.

IV. LOGICAL QUANTUM CIRCUITS

In the previous sections, we have discussed how quantum circuits are attacked by crucial noises with Clifford components. Meanwhile, with the QEC protocol and the fact that Clifford gates are realized transversally, circuits involving more logical qubits and operations can be built in an FT way. It is natural to examine the performance of the Steane code in these higher-level circuits. To present its preservation for quantum information, we will select two appropriate examples for our later simulations in this section.

A. Logical CNOT gate

The logical CNOT gate is deservedly the second step after the establishment of one logical qubit [8,52]. A simple but typical example is the realization of two-qubit entanglement such as the preparation of the Bell state [53], which is a key resource in universal quantum computation. We show the logical version of the circuit for two-qubit entanglement in Fig. 3. After encoding two logical $|0\rangle_L$ and an optional round of QEC, we use single-qubit rotations R_L^1 and R_L^2 for two logical qubits, respectively, of any initial state in the Clifford set

$$\{|0\rangle_L, |1\rangle_L, |+\rangle_L, |-\rangle_L, |+i\rangle_L, |-i\rangle_L\}. \qquad (25)$$

The following logical CNOT gate, which can be realized transversally with the decomposition in Eq. (5) on the physical level, will transform the initial state to our final state, either entangled or still separable. In the end, we need to measure the fidelity of the final state in order to assess the performance of the logical CNOT gate.

According to the logical circuit, the ideal final state is given by

$$|\psi_f\rangle_L = U_{2e}|0\rangle_{L,1}|0\rangle_{L,2}, \qquad U_{2e} \equiv \text{CNOT}_{12}R_L^2 R_L^1, \qquad (26)$$
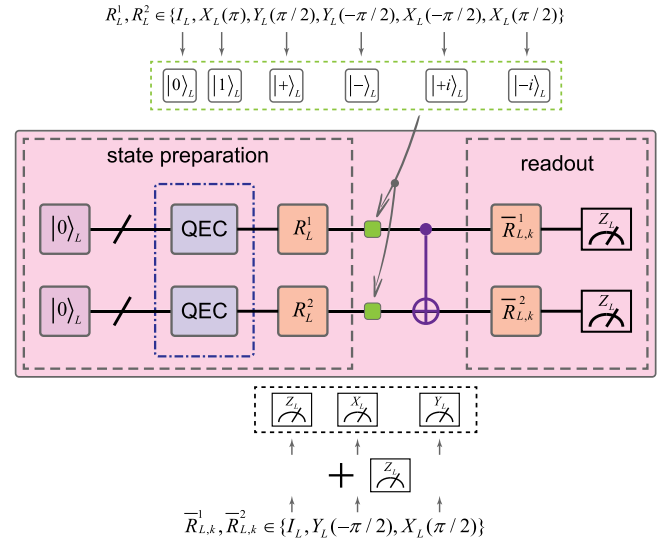

FIG. 3. The circuit for the CNOT operation between two logical qubits. The encoding and QEC modules are presented in Fig. 2 in more detail. Here R_L^1 and R_L^2 are chosen from the six logical operators on the top to rotate each logical qubit to any Clifford state, and the prepared initial state is shown by the two small green boxes. After the logical CNOT gate, Pauli Z_L measurements together with the suitable rotation $\bar{R}_{L,k}^1$ or $\bar{R}_{L,k}^2$ can read out any logical Pauli operator, which provides enough information for the fidelity of the final state.

with the corresponding logical projector

$$P_f = |\psi_f\rangle_L \langle\psi_f|_L$$

$$= U_{2e}\frac{I_{L,1} + Z_{L,1}}{2}\frac{I_{L,2} + Z_{L,2}}{2}U_{2e}^\dagger$$

$$= \frac{1}{4}(I_{L,1} + U_{2e}Z_{L,1}U_{2e}^\dagger)(I_{L,2} + U_{2e}Z_{L,2}U_{2e}^\dagger), \qquad (27)$$

and the fidelity between a state ρ and $|\psi_f\rangle_L$ follows as

$$F_f = \langle P_f \rho \rangle = \frac{1}{4}\langle(I_{L,1} + U_{2e}Z_{L,1}U_{2e}^\dagger)(I_{L,2} + U_{2e}Z_{L,2}U_{2e}^\dagger)\rangle. \qquad (28)$$

For the case of a separable final state, where we take $|1,0\rangle_L \to |1,1\rangle_L$ as an example, the fidelity in Eq. (28) reduces to a simple expression as

$$F_{11} = \frac{1}{4}\langle(I_{L,1} - Z_{L,1})(I_{L,1} - Z_{L,2})\rangle, \qquad (29)$$

which can be obtained by measuring Z_L of two logical qubits directly. Because of the fact that the logical circuit has been finished, we can destructively measure all data qubits to find the distance d to the ideal final state [8]. We come to the logical result consistent with the target if $d \leq 1$, where one possible physical error is allowed.

However, detecting the fidelity of the final state with two-qubit entanglement is a little bit troublesome. If we begin with the initial state $|+, 0\rangle_L$, the Bell state $(1/\sqrt{2})(|0, 0\rangle_L + |1, 1\rangle_L)$ will be targeted. Note that the fidelity in Eq. (28) becomes $\frac{1}{4}\langle(I + Z_{L,1}Z_{L,2})(I + X_{L,1}X_{L,2})\rangle$, but our logical circuit cannot measure $Z_{L,1}Z_{L,2}$ and $X_{L,1}X_{L,2}$ in a nondemolitional way. In fact, the unavoidable sequential measurements of $Z_{L,1}$ and $Z_{L,2}$ will lead to the collapse of the final state, which changes the measurement outcome of $X_{L,1}X_{L,2}$. Instead, we can expand the fidelity as

$$F_{\text{Bell}} = \frac{1}{4}(1 + \langle Z_{L,1}Z_{L,2}\rangle + \langle X_{L,1}X_{L,2}\rangle - \langle Y_{L,1}Y_{L,2}\rangle), \quad (30)$$

where the three expected values of logical operators are from three independent groups of noisy circuit samples. In fact, the fidelity of any possible final state can be expressed in a form that is similar to Eq. (29) or (30). Thus we can further discuss the performance over different input states.

B. Logical Bernstein-Vazirani algorithm

Next, we will demonstrate that the Steane code can protect the quantum information on the algorithm level. The Bernstein-Vazirani (BV) algorithm [27,54] is an appropriate candidate for the following reasons: First, all quantum gates in the algorithm are Clifford gates, which can be directly fed to our simulations. Second, the number of logical qubits and CNOT gates in the oracle of the algorithm can be adjusted arbitrarily, which provides some degrees of freedom for our analysis. Last, the algorithm can realize a practical function with a polynomial improvement from $O(N)$ of the classical computer to $O(1)$.

As shown in Fig. 4, the logical quantum circuit for the BV algorithm contains $N_{\text{ora}} + 1$ logical qubits with the oracle of an N_{ora}-bit string c_{in}. The goal is to determine c_{in} with one query of the oracle, and we will briefly explain how the circuit works.

With the CNOT gates controlled by N_{ora} data qubits $|x\rangle$ and targeting the ancillary qubit $|x_a\rangle$, the oracle keeps $|x\rangle$ (x is an N_{ora}-bit string) while it maps $|x_a\rangle$ to $|x_a \oplus (c_{\text{in}} \cdot x)\rangle$. Here the operations are performed over integers modulo 2. By setting only the nth bit of x as 1 and the others as 0, we can extract the nth bit of c_{in} from the Z_L measurement of the ancillary qubit. Furthermore, the superposition state prepared by the logical Hadamard gates before the oracle contains all information of c_{in}, which can be read out by the Hadamard gates after the oracle and the subsequent Z_L measurements of N_{ora} data qubits. Ideally, the result c_{out} will be consistent with c_{in}. Therefore, we can finish the whole algorithm in one round of the circuit. With enough samples, the success rate of the logical algorithm can be calculated.
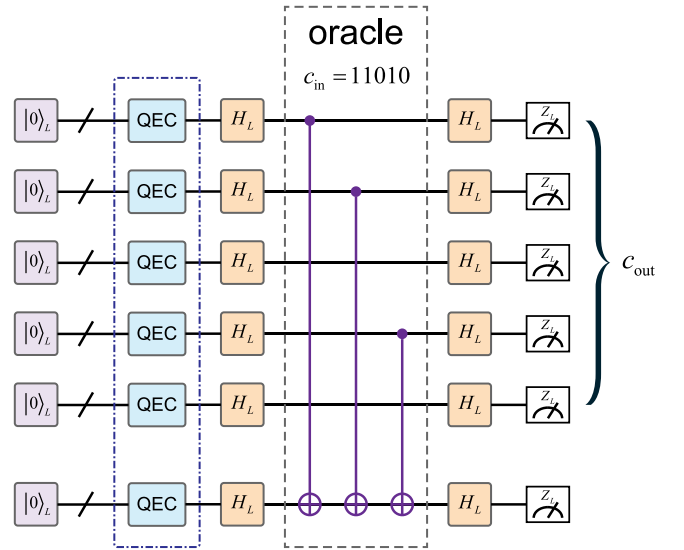

FIG. 4. The logical circuit for the Bernstein-Vazirani algorithm. An example with five-bit oracle $c_{\text{in}} = 11010$ is shown. The top five logical qubits serve as data qubits while the bottom one is the ancillary qubit. The logical modules are similar to those in Fig. 3. If the algorithm is protected successfully, the logical result c_{out} will be consistent with c_{in}.

V. NUMERICAL RESULTS OF LOGICAL PERFORMANCES

In this section, we will present the performance of logical circuits protected by the Steane code in the above three levels, i.e., a single logical qubit, two-qubit logical CNOT gates, and the logical BV algorithm. The simulations are mainly based on the Python package PECOS [55,56], which is an efficient numerical tool for Clifford circuits.

A. Single-qubit protection

Before we perform the simulations, several parameters should be carefully chosen. We can solve Eqs. (9) and (11) linearly to obtain a pulse solution in a large range of these parameters; however, the availability of experiments and the stability of the solution must be considered. Specifically, the laser power, which is directly connected to the Rabi frequency Ω, is an important factor of the former, while the MS-gate infidelity δF belongs to the latter. We recall that the infidelity emerges only when the noises are added.

For simplicity, the motional-mode frequencies are supposed to change as $\omega_k \rightarrow \omega_k + \delta\omega$, which contributes to the noise. Certainly, the actual drift of ω_k could be more complicated, but the underlying stray field [57] can cause a ratio of the drifts of different motional-mode frequencies. If needed, the ratio can be measured in experiments. Moreover, the ratio does not influence the qualitative results, so the uniform drift $\delta\omega$ here is quite reasonable. In this

subsection, we test the infidelity with $\delta\omega = 3$ kHz. Additionally, it is obvious that Ω and δF change with different ion pairs (i_1, i_2) and Ω also changes during the gate time. To make a conservative estimate, we choose the maxima of Ω and δF to be evaluated.

Now we discuss the specific parameters. For the gate time τ and the pulse segments N_{seg}, we expect lower values, but solutions with good quality are usually obtained when they exceed some thresholds. With some numerical explorations, we take $\tau = 400$ μs and $N_{seg} = 4N + 20$ for each ion pair in the following simulations. In the case of one logical qubit, the ion number is $N = 11$ because of the existing seven data qubits, two ancillary qubits, and two buffer ions on the edge of the chain. Excluding the buffer ions, we mark the other ions from left to right with 1 to 9. Another parameter, the COM trapping frequency, does not affect the result obviously on the premise of the formation of a stable ion chain, when a proper ratio of ω_x and ω_z [58] is realized. We take $\omega_x = 1500 \times 2\pi$ kHz and $\omega_z = 100 \times 2\pi$ kHz, which are suitable for numerical experiments in our calculations.

However, the quality of the solution is quite sensitive to the laser detuning μ. As μ changes around the spectrum of the radial modes, the maxima of Ω and δF defined above are presented in Fig. 5. Although Ω and δF show a jumping characteristic when μ changes, good solutions appear around two centers near both ends of the radial-mode spectrum. In the middle of the spectrum, Ω and δF become so bad that the data points exceed the range of the y axis. Here we choose $\mu = 1503 \times 2\pi$ kHz with a nice quality.

As the parameters have been set up and the laser pulses have been calculated, we can move on to the noise decomposition. To illustrate how the noise components depend on the external error source, we plot the curves of different coefficients in Eqs. (21) and (24) as a function of $\delta\omega$ for the ion pair (8, 9), which is shown in Fig. 6. It is obvious that

FIG. 6. Noise coefficients under different drifts of motional-mode frequencies. The values of noise components are based on (a) Clifford decomposition and (b) Pauli twirling approximation. Here the ion pair $(8, 9)$ is taken as an example, and the cases for other pairs are similar. Negative coefficients appear with the components of $X_8 I_9$ and $X_8 X_9$ in the Clifford decomposition.

negative coefficients are inevitable in the Clifford decomposition, and thus simulations based on quasiprobability are necessary with the method in Ref. [21]. The tendency of each curve is similar to the infidelity curve, while the difference between p_{XI} (p'_{XI}) and p_{IX} (p'_{IX}) shows that the ions are affected by the noise unevenly.

Now that the noise coefficients for each ion pair have been prepared, we can put them into our QEC simulator. First we use the protocol in Fig. 2 to test the performance of one single logical qubit. The logical infidelity for $|0\rangle_L$ calculated with the three noise models in Sec. III as a function of $\delta\omega$ is shown in Fig. 7. For comparison, the grey dashed line is plotted to show the averaged physical infidelity for all ion pairs. When the Pauli depolarizing model is applied, we decide the phenomenological error probability $p_{i_1 i_2}$ for the ion pair (i_1, i_2) according to Eq. (14), where the infidelity can be calculated by Eq. (10) since we know the residual entanglement from the laser pulses. Each data point is obtained by 5×10^6 samples of circuits for good accuracy.

In Fig. 7, we can see that the influence of our realistic models is not so severe as the common depolarizing model predicts. In fact, the logical infidelity based on the depolarizing channel is about four times worse than that from the Clifford decomposition or PTA. The explanation for this is that the noise channels for MS gates are always X rotations, which are not so destructive as Y or Z rotations in the depolarizing model. Meanwhile, our two different models for noisy MS gates give results with good consistency, while the small difference between the green line and the pink line can be covered by the error bars. From the previous discussion in Sec. III, we know that the Clifford decomposition gives unbiased results, but requires more samples to achieve a targeted uncertainty because of the negative components in the quasiprobability distribution. On the contrary, PTA needs less circuit samples, while the results may deviate from the true values. Here we discover
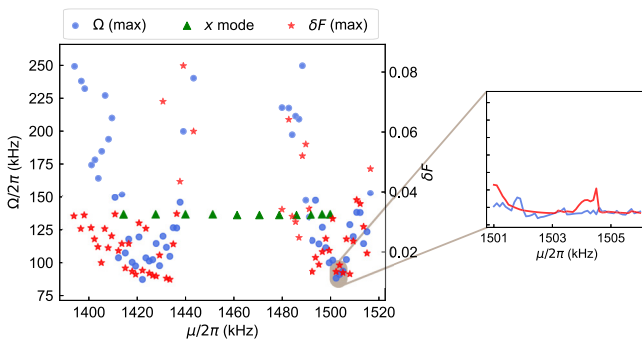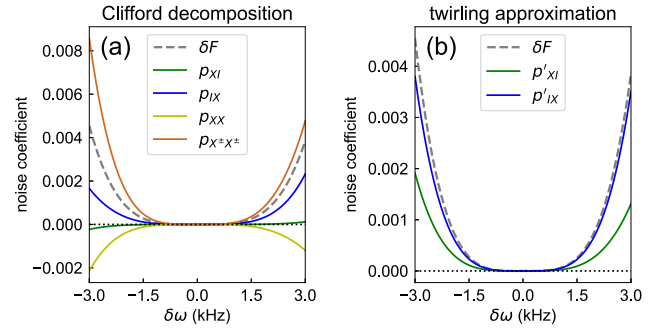

FIG. 5. Maxima of the Rabi frequency and the physical infidelity under different detunings. Data points with lower Ω and δF correspond to better solutions. The detuning is carefully selected from the right pit of points, with more detailed scanning shown in the inset, where the ticks of both y axes are the same as in the main figure.
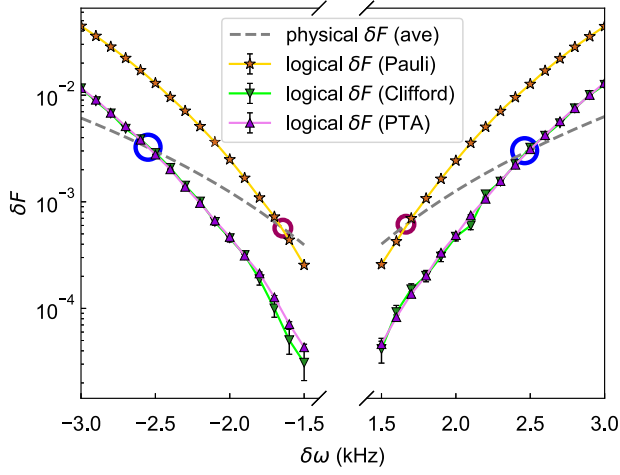
FIG. 7. Infidelity curves for $|0\rangle_L$ with different noise models. The motional-mode drift is scanned in $([-3, -1.5] \cup [1.5, 3])$ kHz, while the data with $|\delta\omega| < 1.5$ kHz are omitted due to the very low infidelity. The Clifford decomposition and PTA give almost the same results, which are significantly lower than the infidelity calculated by the common Pauli depolarizing model. The averaged physical infidelity is also shown for reference, which produces the red and blue crossing points that represent the break-even point for our MS noise models and the depolarizing channels, respectively.

that PTA is a quite good approximation in our QEC circuits and thus it will be adopted for convenience in the following simulations. In addition, with the knowledge of the standard derivation of the binomial distribution, it can be estimated that 10^6 samples are enough for each data point with PTA.

Another message, i.e., the break-even point [10,59], lies in the crossing points marked in Fig. 7. When the noise in the system is weaker than the point, the infidelity of the logical qubit will be less than that of the physical qubit, resulting in effective protection of quantum information with QEC. It can be seen that the infidelity of the MS gate with our noise models on the break-even point is about 3×10^{-3} with the corresponding $\delta\omega \approx 2.5$ kHz, while the results of the depolarizing model are $\delta F = 5 \times 10^{-4}$ and $\delta\omega \approx 1.6$ kHz. Therefore, the infidelity threshold is almost one order higher for the MS noise.

In fact, the nonuniformity of the noise on the ions can be utilized for better performance of the logical qubit. In Fig. 8(b), the noise coefficient p'_{XI} in Eq. (24) for each ion pair (i_1, i_2) is shown, and it is obvious that some MS gates are more noisy. As stated above, we directly arrange the qubits with numbers in Fig. 1(a) according to the blue ion chain in Fig. 8(b) to obtain the results in Fig. 7. Meanwhile, MS gates on different ion pairs with the same error rate will also contribute differently to the final logical infidelity. Intuitively, the stabilizer qubit 8 produces most logical errors because it is used in all MS gates during many
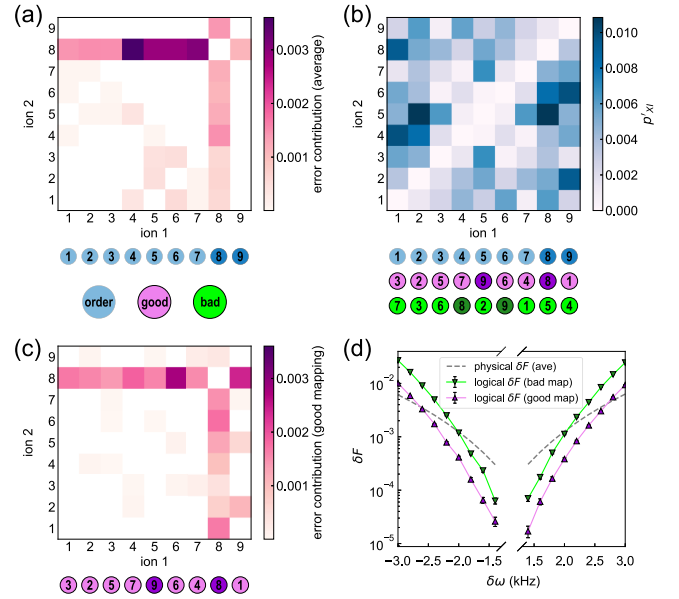

FIG. 8. Ion mapping based on the different influence of qubits and the nonuniformity of the noise coefficients. Ion chains with different colors represent different numbering rules of qubits and the darker circles denote the ancillary qubits. The numerical results are obtained with $\delta\omega = 3$ kHz. (a) The logical error contribution from physical $X_{i_1} I_{i_2}$ of different MS gates. The stabilizer qubit 8 produces most logical errors. (b) Noise coefficient p'_{XI} for each ion pair, which shows some nonuniformity. (c) The logical error contribution after the good mapping. Some critical error sources are mitigated. (d) Infidelity curves for two mapping ways, with a ratio near three.

rounds of stabilizer readout, which can be seen in Fig. 1(b). To prove our prediction, we assume the same probability p'_{XI} or p'_{IX} for each ion pair, which is obtained by averaging the probabilities on all ion pairs, when the external noise parameter is set to $\delta\omega = 3$ kHz. Then we count the samples with both physical errors $X_{i_1} I_{i_2}$ and logical errors. The result divided by the sample number gives the error contribution of the ion pair (i_1, i_2) to the logical qubit.

As shown in Fig. 8(a), MS gates with the stabilizer qubit indeed contribute to most logical errors, especially when the error occurs on the data qubit entangled with the stabilizer qubit. This fact can be explained by some simple analysis of the stabilizer circuit in Fig. 1(b). If an X error appears on the stabilizer qubit, it cannot spread to other qubits and its influence will terminate on the immediate stabilizer readout. On the contrary, the X error on the data qubit stays in the data qubits till the final logical readout and it may become a dangerous Z error after a $Y(-\pi/2)$ gate. Furthermore, it can be observed that, when entangled with the stabilizer qubit, qubit 4 damages the logical qubit most, qubits 5, 6, 7 follow, and then qubits 1, 2, 3. The reason can be reduced to the frequency of occurrence of the data qubit in the QEC circuit, which can be seen in Fig. 1(a).

As a consequence, we manage to improve the logical performance by distributing the ions with a lower infidelity to the dangerous qubits. Specifically, we choose one row of the noise distribution with the minimum averaged p'_{XI} in Fig. 8(b) and set the row number i_2 as the stabilizer qubit. In the selected row, the ions with lower p'_{XI} in Fig. 8(b) are mapped to the qubits with a higher error contribution in Fig. 8(a). Finally we obtain the purple ion chain, and the corresponding error contribution in Fig. 8(c) avoids several awful values in Fig. 8(a). Here we note that the actual noise distribution we adopt in our calculations is just like Fig. 8(b) but it is produced by selecting the larger value of each cell in the distributions of $\delta\omega = 3$ kHz and $\delta\omega = -3$ kHz, in order to fight against the motional-mode drift in both directions. Conversely, we can also find a mapping way for a bad logical performance. The infidelity curves in these two cases are shown in Fig. 8(d), where the bad ion chain gives an infidelity almost three times as much as the good one. As a consequence, ion mapping is an effective way to improve the logical performance, which will be adopted by default in the following simulations.

So far we have not considered the influence of other noise sources. Here we take the depolarizing noise of single-qubit gates as an example. In experiments, the infidelity of single-qubit gates can be controlled to $\delta F_s < 0.01\%$ [16,60] and from Appendix B we know the probability in the depolarizing model is $p_s = \frac{3}{2}\delta F$. With noise comparable to or worse than the current experimental conditions, the logical performance produced by the

simulations is shown in Fig. 9. The blue curve and the red curve can represent the trapped-ion hardware with realistic parameters, which do not deviate from the purple curve without single-qubit noise, especially when the two-qubit noise is dominant. We can only see a tiny shift of the break-even point. For comparison, if the single-qubit gates are too noisy, as the yellow curve, the break-even point will disappear because the errors from single-qubit gates overwhelm. Therefore, the current hardware provides safe noise parameters of single-qubit gates, hence the infidelity is still controlled mainly by the two-qubit gates. Other noises, such as the decoherence of idle qubits and the ion heating [33,61], show a similar behavior. These noises will be omitted so that we focus on the critical two-qubit noise hereafter.

B. Two-qubit CNOT operation

Let us now consider the performance of the logical CNOT gate. Similar to the one-qubit case, the infidelity curve with varying $\delta\omega$ can present resilience to noise. As discussed above, we need to choose a particular state to demonstrate the infidelity curve. Here the result of the initial state $|+, +i\rangle_L$, which produces an entangled final state, is shown in Fig. 10(a). Some modified parameters can be seen in Table I. In our simulation, the ions are first divided into two blocks with nine physical qubits each for the two logical qubits; then they are mapped with the previous method in each block for higher logical fidelity. We compare the curves for the CNOT circuits in Fig. 3 with or without a QEC cycle. The FT characteristic is obvious in the figure, with a large $\delta\omega$ range where the logical infidelity $\delta F_{|+, +i\rangle}$ is lower than the infidelity of physical MS gates. For the case
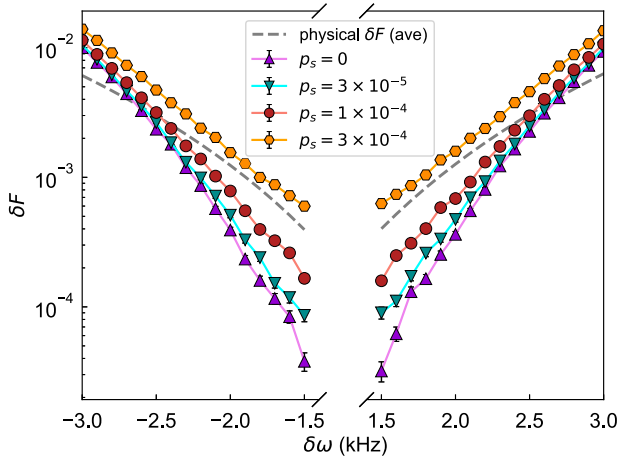

FIG. 9. Infidelity curves with noise from single-qubit gates. Different curves denote different error rates of single-qubit gates, while the purple curve is for the case without any single-qubit noise for comparison. Each curve is still the infidelity as a function of the noise parameter $\delta\omega$ for MS gates with the PTA noise model. The current hardware is usually between the blue and the red curves, with no obvious changes from the purple curve near the break-even point. However, if the single-qubit noise is as severe as the yellow curve, there will no longer be a break-even point.
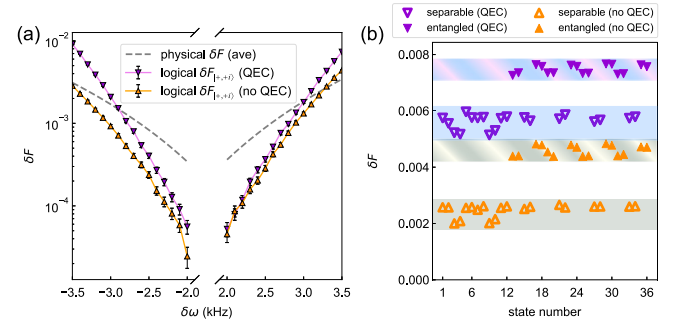

FIG. 10. The performance of the logical CNOT gate. The simulations are based on the PTA noise model. (a) The fidelity of the logical final state from the input $|+, +i\rangle_L$ can surpass the physical counterpart. Here the QEC cycle introduces more logical errors when correcting some existing physical errors, which is the reason why the performance is better for the case without QEC. (b) All 36 Clifford states are tested for the CNOT circuit in Fig. 3. The data of logical infidelity are distributed in different bands for separable and entangled final states, respectively. It is shown that the errors influence the circuits more when preparing entangled states.

TABLE I. Some parameters used in the simulations. The columns contain the cases for the logical CNOT operation and the BV algorithm of both physical and logical versions. The ion chain always includes two buffer ions, while other $N - 2$ ions serve as qubits. For the logical BV algorithm, the radial frequency ω_x has to be increased to maintain a stable ion chain. In addition, the detuning μ is scanned for a lower Rabi frequency and better infidelity.

| | | BV algorithm | | | |
| | | $c_{in} = 110$ | | $c_{in} = 11010$ | |
Parameters	CNOT	Physical	Logical	Physical	Logical
N	20	6	38	8	56
$\omega_x/2\pi$ (kHz)	1500	1500	2000	1500	2500
$\mu/2\pi$ (kHz)	1403.85	1502.2	2000.9	1445.8	2505.2

FIG. 11. The infidelity curves for the logical BV algorithm. The simulations are based on the PTA noise model. Two oracles $c_{in} = 110$ and $c_{in} = 11010$ are tested in panels (a) and (b), respectively. With the Steane code, the failure rate of the final result can be lower than the infidelity of MS gates and that of the physical-qubit version of the same circuit for the BV algorithm. Apparently, the QEC cycle causes more errors to the logical circuit, while its significance is explained with the numerical result in Fig. 12.

without QEC, the fault tolerance comes from the establishment of logical qubits themselves, which cannot be destroyed by one single-qubit error. It seems that the QEC causes a worse result, but actually the QEC clears some accumulated errors in the encoding circuit, which presents its effectiveness in deeper circuits. We will further discuss this problem in the subsequent section.

In order to analyze the logical CNOT operation from a more comprehensive perspective, we calculate the infidelity for all 36 possible initial Clifford states with $\delta\omega = 3.5$ kHz. The single-qubit states are numbered as j_1 and j_2 from 1 to 6 in the order of Eq. (25) for the two qubits, and the two-qubit state is numbered as $j = 6(j_1 - 1) + j_2$. After deriving the fidelity expression for each state with Eq. (28), the 36 final states are divided into 20 separable states and 16 entangled states. In Fig. 10(b), the logical infidelity for the 36 states are presented, with hollow triangles for separable states and solid triangles for entangled states. We find that, in both cases, more logical errors occur in the preparation of the entangled states. This can be explained by the sensitivity of the logical fidelity, such as the expression in Eq. (28), to more physical errors. Overall, the logical CNOT gate can be realized fault-tolerantly, while the errors attack the circuit a little more while preparing the entangled states.

C. Multi-qubit BV algorithm

The next level to assess the performance of the Steane code is the logical version of the BV algorithm. We use the simulator to test the circuit in Fig. 4. Finally, the probability of obtaining a wrong result of the algorithm is shown in Fig. 11, with the varying motional-mode drift as before. The oracle c_{in} in the algorithm is chosen as 11010 or 110 in our simulations. Here, the parameters for each case are properly selected, which are summarized in Table I. Except for some specific differences of the infidelity values, which is due to the pulse calculations under different parameters, the qualitative results are the same for the two oracles here
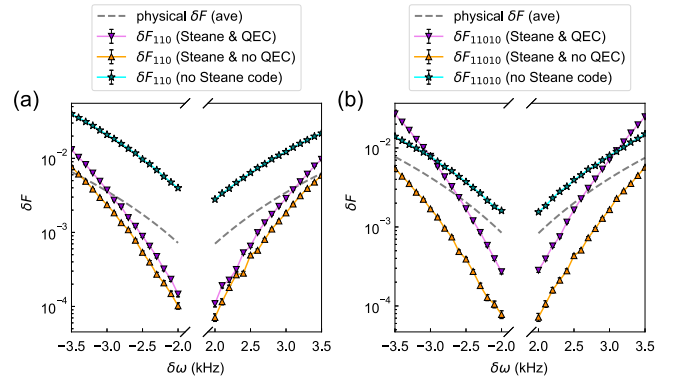
and also other oracles. The influence of the QEC cycle is analyzed as the CNOT circuit and it is shown that more errors are seemingly introduced.

In order to demonstrate the advantage of the logical encoding, the infidelity curves for the circuit in Fig. 4 are compared to that for the physical version of the circuit. It is obvious that, in Fig. 11, the blue curves that represent the result without the logical encoding are worse. We can further observe that these curves are parallel to and higher than the physical infidelity curves of MS gates, which shows the absence of fault tolerance. In contrast, the curves for the results with the Steane code can be lower than the physical infidelity when the external noise is not too strong. In other words, the Steane code successfully protects the BV algorithm.

However, we can find more information which is not obvious when different oracles are tested. For c_{in} with length of five, there are $2^5 = 32$ choices. The count of 1 in the oracle denotes the number of logical CNOT gates. We simulate the circuits for all 32 oracles under $\delta\omega = 2.5$ kHz and the results are plotted in Fig. 12. It can be seen that the infidelity increases linearly with the number of CNOT gates, especially when the QEC cycle is omitted. The results can be explained as follows. The intercept is the fidelity without any CNOT operators, so the logical errors come from the encoding circuit with one optional round of QEC. Meanwhile, the slope is the additional infidelity from one logical CNOT gate on average.

Although QEC causes more logical errors apparently, it clears many potential physical errors in the encoding section, which are not exposed immediately. As the subsequent logical operators accumulate, some physical errors
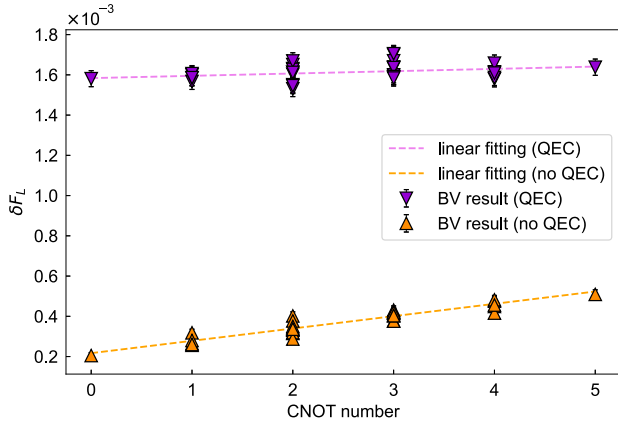
FIG. 12. The performance of all 32 BV oracles with five logical qubits. The results with one round of QEC show a larger intercept but a much smaller slope, which means that QEC introduces some logical errors while also clearing many potential and dangerous physical errors. This reveals that, for deeper logical quantum circuits, the effectiveness of QEC will emerge. In addition, the infidelity dispersion of a given CNOT number comes from the nonuniformity of the noise on different ion pairs.

continue to occur. Combined with the previous physical errors in the encoding circuit, these new errors will lead to wrong logical outputs. Therefore, if the QEC cycle is cancelled, the final infidelity will be very sensitive to the logical CNOT operations. The slope of the fit is 1.1×10^{-5} or 6.1×10^{-5} for the cases with or without the QEC cycle, respectively. Accordingly, in the more complicated logical circuits, QEC cycles will improve the logical infidelity of the final result. Of course, the frequency and the location of the inserted QEC cycle should be carefully optimized for a better logical performance.

VI. CONCLUSIONS

In this work, we analyze the performance of different logical circuits with the quantum information encoded in the Steane codes based on the trapped-ion system. More specific noise models for MS gates are established, where the hardware parameters are carefully considered for the pulses of MS gates. We explore the logical performance in three levels, i.e., the one-qubit protection, the two-qubit operation, and the multi-qubit BV algorithm. Our simulations indicate that the logical infidelity with realistic noise models is obviously lower than the infidelity with the conventional depolarizing model. In each level, the logical fidelity can surpass the physical fidelity in a large range of external noise parameters, with the break-even point between 10^{-3} and 10^{-2}. Furthermore, the nonuniformity of the noises can be utilized to find a better mapping from ions to qubits, improving the logical fidelity and the break-even point. For the cases of two or more logical qubits, the

QEC cycle leads to some extra errors but also clears many potential physical errors.

Our simulations highlight the importance of the noise model customization for specific and realistic hardware. For different platforms, e.g., neutral atom arrays [6] and superconducting system [4], more information about the noise can also be obtained from the evolution equations of the quantum states. In these pioneering experimental works of QEC, some noise characteristics have been analyzed. However, there is still some space for more accurate noise models, which can be beneficial to mitigate the error rates in the quantum circuits for a better logical performance. In the future, we will broaden the analysis of the noise models in different devices, while also attempting to optimize the scheme of specific gates with knowledge of noise. The exploration will provide more possibility to realize QEC with a larger scale in future experiments.

APPENDIX A: CIRCUITS FOR ENCODING A LOGICAL STATE

In this appendix, we present the detailed encoding circuits in the light purple box of Fig. 2. The circuit with a flag qubit in Fig. 13(a) is for preparing a logical $|0\rangle_L$ state. If the flag is triggered, two weight-three logical operators $Z_{L,1}$ and $Z_{L,2}$ are consecutively read out by the circuit in Fig. 13(b).

APPENDIX B: AVERAGE FIDELITY OF THE DEPOLARIZING CHANNEL

For the depolarizing channel, we are concerned about the relationship between the error probability p and its infidelity because the latter can be calculated by other methods such as from Eq. (10). We consider the general case $\mathcal{E}_{N_q}^{\text{dep}}$ for N_q qubits. The Kraus operators are chosen from the Pauli operators

$$\{I, X, Y, Z\}^{\otimes N_q} \setminus \{I^{\otimes N_q}\}, \tag{B1}$$

with the occurring probability $p/(2^{2N_q} - 1)$ for each operator, while the remaining probability $1 - p$ is for $I^{\otimes N_q}$. When the basis of states is naturally chosen as Pauli strings, the averaged fidelity in the Haar measure [47] is

$$F_q = \frac{1}{d^2(d+1)} \left[\sum_{\sigma_q} \text{Tr}(\sigma_q^\dagger \mathcal{E}_{N_q}^{\text{dep}}(\sigma_q)) + d^2 \right], \tag{B2}$$
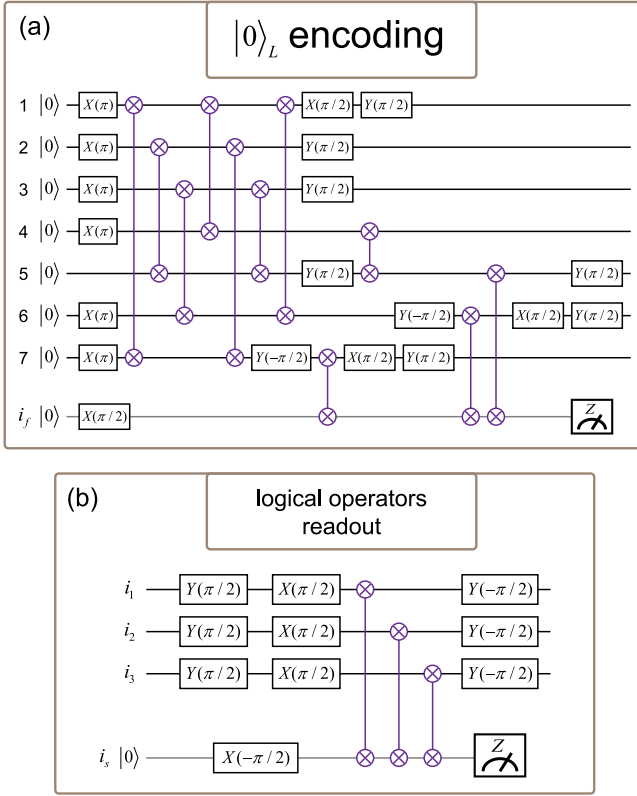
FIG. 13. The circuits used in the encoding module. (a) The initialization circuit for $|0\rangle_L$ with a flag qubit monitoring the possible dangerous errors. (b) Using the circuit, we can read out the information of the most probable physical errors that occurred in the previous encoding circuit. Specifically, two logical operators $Z_{L,1} = Z_1 Z_2 Z_7$ and $Z_{L,2} = Z_2 Z_3 Z_5$ contain the targeted information.

where $d = 2^{N_q}$ is the dimension of the Hilbert space, and σ_q is from d^2 possible N_q-qubit Pauli strings,

$$\sigma_q = \prod_{i=1}^{N_q} \sigma_{j_i}^i, \quad \sigma_{j_i}^i \in \{I, X, Y, Z\}. \tag{B3}$$

Any state ρ after the depolarizing channel $\mathcal{E}_{N_q}^{\text{dep}}$ can be written as

$$\mathcal{E}_{N_q}^{\text{dep}}(\rho) = (1-p)\rho + \frac{p}{d^2-1} \sum_{\sigma_{q'} \neq I^{\otimes N_q}} \sigma_{q'}^\dagger \rho \sigma_{q'}$$

$$= \left(1 - \frac{d^2}{d^2-1}p\right)\rho + \frac{p}{d^2-1} \sum_{\sigma_{q'}} \sigma_{q'}^\dagger \rho \sigma_{q'}. \tag{B4}$$

Then the trace term in Eq. (B2) is given by

$$\sum_{\sigma_q} \text{Tr}(\sigma_q^\dagger \mathcal{E}_{N_q}^{\text{dep}}(\sigma_q))$$

$$= \left(1 - \frac{d^2}{d^2-1}p\right) \sum_{\sigma_q} \text{Tr}(\sigma_q^\dagger \sigma_q)$$

$$+ \frac{p}{d^2-1} \sum_{\sigma_q \sigma_{q'}} \text{Tr}(\sigma_q^\dagger \sigma_{q'}^\dagger \sigma_q \sigma_{q'})$$

$$= (1-p)d^3, \tag{B5}$$

where we have used

$$\sum_{\sigma_q} \text{Tr}(\sigma_q^\dagger \sigma_q) = d^2 \text{Tr}(I_d) = d^3 \tag{B6}$$

and

$$\sum_{\sigma_q \sigma_{q'}} \text{Tr}(\sigma_q^\dagger \sigma_{q'}^\dagger \sigma_q \sigma_{q'})$$

$$= \sum_{\substack{j_1, j_2, \dots, j_{N_q}, \\ j_1', j_2', \dots, j_{N_q}'=0}}^{3} \prod_{i=1}^{N_q} \text{Tr}(\sigma_{j_i}^i \sigma_{j_i'}^i \sigma_{j_i}^i \sigma_{j_i'}^i)$$

$$= \sum_{\substack{j_1, j_2, \dots, j_{N_q}, \\ j_1', j_2', \dots, j_{N_q}'=0}}^{3} \text{Tr}\left(\sigma_{j_1}^1 \sigma_{j_1'}^1 \sigma_{j_1}^1 \sigma_{j_1'}^1 \otimes \sigma_{j_1}^2 \sigma_{j_1'}^2 \sigma_{j_1}^2 \sigma_{j_1'}^2\right.$$

$$\left. \otimes \cdots \otimes \sigma_{j_1}^{N_q} \sigma_{j_1'}^{N_q} \sigma_{j_1}^{N_q} \sigma_{j_1'}^{N_q}\right)$$

$$= \prod_{i=1}^{N_q} \left[\sum_{j_i, j_i'=0}^{3} \text{Tr}(\sigma_{j_i}^i \sigma_{j_i'}^i \sigma_{j_i}^i \sigma_{j_i'}^i)\right]$$

$$= \prod_{i=1}^{N_q} 2^3 = d^3. \tag{B7}$$

Combining Eqs. (B2) and (B4), we obtain the expression of the averaged fidelity as

$$F_q = 1 - \frac{d}{d+1}p. \tag{B8}$$

For the MS gate, we take $d = 4$ in Eq. (B8) to get the result of Eq. (14) in the main text.

APPENDIX C: CLIFFORD DECOMPOSITION OF MS GATES BY THE SUPEROPERATOR

Here we present the derivation of the Clifford decomposition of noisy MS gates given by Eqs. (20) and (21). Because of the fact that the superoperator of the noise

channel $\mathcal{E}_{\mathrm{MS}}^{\mathrm{Clif}}$ can be represented as a 16×16 diagonal matrix $\mathbf{S}_{\mathrm{MS}}$, the 16 nonzero elements can be rearranged as a 4×4 matrix $\bar{\mathbf{S}}_{\mathrm{MS}}$. Observing Eqs. (16) and (19), we can write the full matrix as

$$\bar{\mathbf{S}} = \begin{pmatrix} 1 & 1-\varepsilon_{i_2} & 1-\varepsilon_{i_1} & 1-\varepsilon_+ \\ 1-\varepsilon_{i_2} & 1 & 1-\varepsilon_- & 1-\varepsilon_{i_1} \\ 1-\varepsilon_{i_1} & 1-\varepsilon_- & 1 & 1-\varepsilon_{i_2} \\ 1-\varepsilon_+ & 1-\varepsilon_{i_1} & 1-\varepsilon_{i_2} & 1 \end{pmatrix}, \quad (C1)$$

which describes $\mathcal{E}_{\mathrm{MS}}^{\mathrm{Clif}}$ in the form

$$\left(\mathcal{E}_{\mathrm{MS}}^{\mathrm{Clif}}(\rho) \right)_{mn} = \bar{\mathbf{S}}_{mn} \rho_{mn}. \quad (C2)$$

Essentially, Eq. (C2) is only a tight form of Eq. (18). Therefore, we can directly decompose $\bar{\mathbf{S}}$ instead of $\mathbf{S}_{\mathrm{MS}}$ to obtain the related Clifford channels.

Considering the diagonal property of $\mathbf{S}_{\mathrm{MS}}$ in the basis of $|\pm\rangle^{\otimes 2}$ again, we focus on the Clifford rotations around the x axis. Let us start with the single-qubit rotation

$$X(\theta) = \begin{pmatrix} e^{-i\theta/2} & 0 \\ 0 & e^{i\theta/2} \end{pmatrix}, \quad (C3)$$

where $\theta \in \{0, \pm\pi/2, \pi\}$ for Clifford channels. Furthermore, we consider two such rotations acting on two qubits with the matrix

$$\begin{aligned} & X_{i_1}(\theta_1) X_{i_2}(\theta_2) \\ &= \begin{pmatrix} e^{-i\theta_1/2} & 0 \\ 0 & e^{i\theta_1/2} \end{pmatrix} \otimes \begin{pmatrix} e^{-i\theta_2/2} & 0 \\ 0 & e^{i\theta_2/2} \end{pmatrix} \\ &= \begin{pmatrix} e^{-i(\theta_1+\theta_2)/2} & 0 & 0 & 0 \\ 0 & e^{i(-\theta_1+\theta_2)/2} & 0 & 0 \\ 0 & 0 & e^{i(\theta_1-\theta_2)/2} & 0 \\ 0 & 0 & 0 & e^{i(\theta_1+\theta_2)/2} \end{pmatrix}. \end{aligned}$$
$$(C4)$$

By calculating the evolution of the two-qubit state ρ_i under the unitary operation straightforwardly, we can obtain the corresponding reduced superoperator

$$\bar{\mathbf{S}}_{X_\theta X_\theta} = \begin{pmatrix} 1 & e^{-i\theta_2} & e^{-i\theta_1} & e^{-i(\theta_1+\theta_2)} \\ e^{i\theta_2} & 1 & e^{i(-\theta_1+\theta_2)} & e^{-i\theta_1} \\ e^{i\theta_1} & e^{i(\theta_1-\theta_2)} & 1 & e^{-i\theta_2} \\ e^{i(\theta_1+\theta_2)} & e^{i\theta_1} & e^{i\theta_2} & 1 \end{pmatrix}. \quad (C5)$$

In Eqs. (C1) and (C5), the following conditions are satisfied automatically even with any linear combination of real

coefficients:

$$\begin{aligned} (\bar{\mathbf{S}})^\dagger &= \bar{\mathbf{S}}, \\ \bar{\mathbf{S}}_{11} &= \bar{\mathbf{S}}_{11}^* = \bar{\mathbf{S}}_{22} = \bar{\mathbf{S}}_{33} = \bar{\mathbf{S}}_{44}, \\ \bar{\mathbf{S}}_{12} &= \bar{\mathbf{S}}_{34}, \\ \bar{\mathbf{S}}_{13} &= \bar{\mathbf{S}}_{24}, \end{aligned} \quad (C6)$$

while they are also true for $\bar{\mathbf{S}}_{X_\theta X_\theta}$. In addition, the elements in $\bar{\mathbf{S}}$ are real numbers, resulting in only five free parameters to be determined:

$$\mathrm{Re}(\bar{\mathbf{S}}_{11}), \ \mathrm{Re}(\bar{\mathbf{S}}_{12}), \ \mathrm{Re}(\bar{\mathbf{S}}_{13}), \ \mathrm{Re}(\bar{\mathbf{S}}_{14}), \ \mathrm{Re}(\bar{\mathbf{S}}_{23}). \quad (C7)$$

We can easily find four Clifford $X_\theta X_\theta$ channels with all elements real, which are given by

$$\begin{aligned} \bar{\mathbf{S}}_{II} &= \begin{pmatrix} 1 & 1 & 1 & 1 \\ 1 & 1 & 1 & 1 \\ 1 & 1 & 1 & 1 \\ 1 & 1 & 1 & 1 \end{pmatrix}, \\ \bar{\mathbf{S}}_{XI} &= \begin{pmatrix} 1 & 1 & -1 & -1 \\ 1 & 1 & -1 & -1 \\ -1 & -1 & 1 & 1 \\ -1 & -1 & 1 & 1 \end{pmatrix}, \\ \bar{\mathbf{S}}_{IX} &= \begin{pmatrix} 1 & -1 & 1 & -1 \\ -1 & 1 & -1 & 1 \\ 1 & -1 & 1 & -1 \\ -1 & 1 & -1 & 1 \end{pmatrix}, \\ \bar{\mathbf{S}}_{XX} &= \begin{pmatrix} 1 & -1 & -1 & 1 \\ -1 & 1 & 1 & -1 \\ -1 & 1 & 1 & -1 \\ 1 & -1 & -1 & 1 \end{pmatrix}, \end{aligned} \quad (C8)$$

with at least one other channel to be found. Fortunately, the combination of two channels can eliminate all imaginary part of the elements as

$$\begin{aligned} \bar{\mathbf{S}}_{X^+X^+} &= \begin{pmatrix} 1 & -i & -i & -1 \\ i & 1 & 1 & -i \\ i & 1 & 1 & -i \\ -1 & i & i & 1 \end{pmatrix}, \\ \bar{\mathbf{S}}_{X^-X^-} &= \begin{pmatrix} 1 & i & i & -1 \\ -i & 1 & 1 & i \\ -i & 1 & 1 & i \\ -1 & -i & -i & 1 \end{pmatrix}, \quad (C9) \\ \frac{1}{2}(\bar{\mathbf{S}}_{X^+X^+} + \bar{\mathbf{S}}_{X^-X^-}) &= \begin{pmatrix} 1 & 0 & 0 & -1 \\ 0 & 1 & 1 & 0 \\ 0 & 1 & 1 & 0 \\ -1 & 0 & 0 & 1 \end{pmatrix}. \end{aligned}$$

We now attempt to decompose $\bar{\mathbf{S}}$ with the above channels by

$$\bar{\mathbf{S}} = p_{II}\bar{\mathbf{S}}_{II} + p_{XI}\bar{\mathbf{S}}_{XI} + p_{IX}\bar{\mathbf{S}}_{IX} + p_{XX}\bar{\mathbf{S}}_{XX}$$
$$+ p_{X^\pm X^\pm}\left[\frac{1}{2}(\bar{\mathbf{S}}_{X^+X^+} + \bar{\mathbf{S}}_{X^-X^-})\right]. \quad (C10)$$

Finally, we only need to match the five parameters in Eq. (C7) on both sides of Eq. (C10):

$$p_{II} + p_{XI} + p_{IX} + p_{XX} + p_{X^\pm X^\pm} = 1,$$
$$p_{II} + p_{XI} - p_{IX} - p_{XX} = 1 - \varepsilon_{i_2},$$
$$p_{II} - p_{XI} + p_{IX} - p_{XX} = 1 - \varepsilon_{i_1}, \quad (C11)$$
$$p_{II} - p_{XI} - p_{IX} + p_{XX} - p_{X^\pm X^\pm} = 1 - \varepsilon_+,$$
$$p_{II} - p_{XI} - p_{IX} + p_{XX} + p_{X^\pm X^\pm} = 1 - \varepsilon_-,$$

where $\frac{1}{2}p_{X^\pm X^\pm} = p_{X^+X^+} = p_{X^-X^-}$. Solving the linear equations directly, we can obtain the results in Eq. (21).

APPENDIX D: CHANNELS AND COEFFICIENTS OF MS GATES IN PTA

In this appendix, we provide the calculations for the coefficients in Eq. (24) by twirling the quantum channel $\mathcal{E}_{\mathrm{MS}}^{\mathrm{Clif}}$ over the Pauli basis. In the matrix representation in Eq. (C3), the $\pm\pi/2$ rotation around the x axis is given by

$$X(\pm\pi/2) = \begin{pmatrix} e^{\mp i\pi/4} & 0 \\ 0 & e^{\pm i\pi/4} \end{pmatrix}$$
$$= \frac{1}{\sqrt{2}}\begin{pmatrix} 1 \mp i & 0 \\ 0 & 1 \pm i \end{pmatrix} = \frac{1}{\sqrt{2}}(I \pm X). \quad (D1)$$

Then the two-qubit Kraus operator $X_{i_1}(\pm(\pi/2))X_{i_2}(\pm(\pi/2))$ is equivalent to

$$X_{i_1}\left(\pm\frac{\pi}{2}\right)X_{i_2}\left(\pm\frac{\pi}{2}\right) = \frac{1}{2}(I \pm X_{i_1})(I \pm X_{i_2}), \quad (D2)$$

which is replaced by Kraus operators

$$\{II, X_{i_1}I, IX_{i_2}, X_{i_1}X_{i_2}\} \quad (D3)$$

and the same probability $|\pm\frac{1}{2}|^2 = \frac{1}{4}$ in the PTA [50]. Finally, they are merged with the existing counterparts, resulting in the probabilities from Eqs. (21) to (24).

[1] P. W. Shor, Scheme for reducing decoherence in quantum computer memory, Phys. Rev. A **52**, R2493 (1995).

[2] A. Steane, Multiple-particle interference and quantum error correction, Proc. Math. Phys. Eng. Sci. **452**, 2551 (1996).

[3] A. G. Fowler, M. Mariantoni, J. M. Martinis, and A. N. Cleland, Surface codes: Towards practical large-scale quantum computation, Phys. Rev. A **86**, 032324 (2012).

[4] S. Krinner, N. Lacroix, A. Remm, A. Di Paolo, E. Genois, C. Leroux, C. Hellings, S. Lazar, F. Swiadek, A. Wallraff, *et al.*, Realizing repeated quantum error correction in a distance-three surface code, Nature **605**, 669 (2022).

[5] R. Acharya, I. Aleiner, R. Allen, T. I. Andersen, M. Ansmann, F. Arute, K. Arya, A. Asfaw, J. Atalaya, R. Babbush, *et al.*, Suppressing quantum errors by scaling a surface code logical qubit, Nature **614**, 676 (2023).

[6] D. Bluvstein, S. J. Evered, A. A. Geim, S. H. Li, H. Zhou, T. Manovitz, S. Ebadi, M. Cain, M. Kalinowski, M. D. Lukin, *et al.*, Logical quantum processor based on reconfigurable atom arrays, Nature **626**, 58 (2024).

[7] L. Egan, D. M. Debroy, C. Noel, A. Risinger, D. Zhu, D. Biswas, M. Newman, M. Li, K. R. Brown, M. Cetina, and C. Monroe, Fault-tolerant control of an error-corrected qubit, Nature **598**, 281 (2021).

[8] L. Postler, S. Heußen, I. Pogorelov, M. Rispler, T. Feldker, M. Meth, C. D. Marciniak, P. Schindler, M. Müller, T. Monz, *et al.*, Demonstration of fault-tolerant universal quantum gate operations, Nature **605**, 675 (2022).

[9] C. Ryan-Anderson, J. G. Bohnet, K. Lee, D. Gresh, A. Hankin, J. P. Gaebler, D. Francois, B. Neyenhuis, D. Hayes, R. P. Stutz, *et al.*, Realization of Real-Time Fault-Tolerant Quantum Error Correction, Phys. Rev. X **11**, 041058 (2021).

[10] A. Bermudez, X. Xu, R. Nigmatullin, J. O'Gorman, V. Negnevitsky, P. Schindler, T. Monz, R. Blatt, S. Benjamin, M. Müller, *et al.*, Assessing the Progress of Trapped-Ion Processors Towards Fault-Tolerant Quantum Computation, Phys. Rev. X **7**, 041061 (2017).

[11] A. Bermudez, X. Xu, M. Gutiérrez, S. C. Benjamin, and M. Müller, Fault-tolerant protection of near-term trapped-ion topological qubits under realistic noise sources, Phys. Rev. A **100**, 062307 (2019).

[12] D. M. Debroy, M. Li, S. Huang, and K. R. Brown, Logical performance of 9 qubit compass codes in ion traps with crosstalk errors, Quantum Sci. Technol. **5**, 034002 (2020).

[13] S. Heußen, L. Postler, M. Rispler, I. Pogorelov, C. D. Marciniak, T. Monz, P. Schindler, and M. Müller, Strategies for a practical advantage of fault-tolerant circuit design in noisy trapped-ion quantum computers, Phys. Rev. A **107**, 042422 (2023).

[14] S.-L. Zhu, C. Monroe, and L.-M. Duan, Arbitrary-speed quantum gates within large ion crystals through minimum control of laser beams, Europhys. Lett. **73**, 485 (2006).

[15] Y. Wu, S.-T. Wang, and L.-M. Duan, Noise analysis for high-fidelity quantum entangling gates in an anharmonic linear Paul trap, Phys. Rev. A **97**, 062325 (2018).

[16] C. J. Ballance, T. P. Harty, N. M. Linke, M. A. Sepiol, and D. M. Lucas, High-Fidelity Quantum Logic Gates Using Trapped-Ion Hyperfine Qubits, Phys. Rev. Lett. **117**, 060504 (2016).

[17] S. Puri, L. St-Jean, J. A. Gross, A. Grimm, N. E. Frattini, P. S. Iyer, A. Krishna, S. Touzard, L. Jiang, A. Blais, S. T. Flammia, and S. M. Girvin, Bias-preserving gates with stabilized cat qubits, Sci. Adv. **6**, eaay5901 (2020).

[18] O. Higgott, T. C. Bohdanowicz, A. Kubica, S. T. Flammia, and E. T. Campbell, Improved Decoding of Circuit Noise

and Fragile Boundaries of Tailored Surface Codes, Phys. Rev. X **13**, 031007 (2023).

[19] C. Chamberland and E. T. Campbell, Universal Quantum Computing with Twist-Free and Temporally Encoded Lattice Surgery, PRX Quantum **3**, 010331 (2022).

[20] M. Gutiérrez, L. Svec, A. Vargo, and K. R. Brown, Approximation of realistic errors by Clifford channels and Pauli measurements, Phys. Rev. A **87**, 030302(R) (2013).

[21] R. S. Bennink, E. M. Ferragut, T. S. Humble, J. A. Laska, J. J. Nutaro, M. G. Pleszkoch, and R. C. Pooser, Unbiased simulation of near-Clifford quantum circuits, Phys. Rev. A **95**, 062337 (2017).

[22] C. C. López, A. Bendersky, J. P. Paz, and D. G. Cory, Progress toward scalable tomography of quantum maps using twirling-based methods and information hierarchies, Phys. Rev. A **81**, 062113 (2010).

[23] D. Gottesman, Stabilizer codes and quantum error correction, arXiv:quant-ph/9705052.

[24] A. M. Steane, Error Correcting Codes in Quantum Theory, Phys. Rev. Lett. **77**, 793 (1996).

[25] R. Chao and B. W. Reichardt, Quantum Error Correction with Only Two Extra Qubits, Phys. Rev. Lett. **121**, 050502 (2018).

[26] H. Bombin and M. A. Martin-Delgado, Topological Quantum Distillation, Phys. Rev. Lett. **97**, 180501 (2006).

[27] K. Wright, K. M. Beck, S. Debnath, J. M. Amini, Y. Nam, N. Grzesiak, J.-S. Chen, M. Keesan, C. Monroe, J. Kim, *et al.*, Benchmarking an 11-qubit quantum computer, Nat. Commun. **10**, 5464 (2019).

[28] S. Debnath, N. M. Linke, C. Figgatt, K. A. Landsman, K. Wright, and C. Monroe, Demonstration of a small programmable quantum computer with atomic qubits, Nature **536**, 63 (2016).

[29] P. Schindler, D. Nigg, T. Monz, J. T. Barreiro, E. Martinez, S. X. Wang, S. Quint, M. Chwalla, M. Hennrich, R. Blatt, *et al.*, A quantum information processor with trapped ions, New J. Phys. **15**, 123012 (2013).

[30] A. Sørensen and K. Mølmer, Quantum Computation with Ions in Thermal Motion, Phys. Rev. Lett. **82**, 1971 (1999).

[31] D. Maslov, Basic circuit compilation techniques for an ion-trap quantum machine, New J. Phys. **19**, 023035 (2017).

[32] C. D. Bruzewicz, J. Chiaverini, R. McConnell, and J. M. Sage, Trapped-ion quantum computing: Progress and challenges, Appl. Phys. Rev. **6**, 021314 (2019).

[33] C. J. Trout, M. Li, M. Gutiérrez, Y. Wu, S.-T. Wang, L. Duan, and K. R. Brown, Simulating the performance of a distance-3 surface code in a linear ion trap, New J. Phys. **20**, 043038 (2018).

[34] T. Choi, S. Debnath, T. A. Manning, C. Figgatt, Z.-X. Gong, L.-M. Duan, and C. Monroe, Optimal Quantum Control of Multimode Couplings Between Trapped Ion Qubits for Scalable Entanglement, Phys. Rev. Lett. **112**, 190502 (2014).

[35] Y. Lu, S. N. Zhang, K. Zhang, W. T. Chen, Y. C. Shen, J. L. Zhang, J. N. Zhang, and K. Kim, Global entangling gates on arbitrary ion qubits, Nature **572**, 363 (2019).

[36] E. Magesan, D. Puzzuoli, C. E. Granade, and D. G. Cory, Modeling quantum noise for efficient testing of fault-tolerant circuits, Phys. Rev. A **87**, 012324 (2013).

[37] C. J. Wood, J. D. Biamonte, and D. G. Cory, Tensor networks and graphical calculus for open quantum systems, arXiv:1111.6950.

[38] S.-L. Zhu, C. Monroe, and L.-M. Duan, Trapped Ion Quantum Computation with Transverse Phonon Modes, Phys. Rev. Lett. **97**, 050505 (2006).

[39] T. Olsacher, L. Postler, P. Schindler, T. Monz, P. Zoller, and L. M. Sieberer, Scalable and Parallel Tweezer Gates for Quantum Computing with Long Ion Strings, PRX Quantum **1**, 020316 (2020).

[40] A. R. Milne, C. L. Edmunds, C. Hempel, F. Roy, S. Mavadia, and M. J. Biercuk, Phase-modulated entangling gates robust to static and time-varying errors, Phys. Rev. Appl. **13**, 024022 (2020).

[41] P. H. Leung, K. A. Landsman, C. Figgatt, N. M. Linke, C. Monroe, and K. R. Brown, Robust 2-Qubit Gates in a Linear Ion Crystal Using a Frequency-Modulated Driving Force, Phys. Rev. Lett. **120**, 020501 (2018).

[42] L. Cheng, S.-C. Liu, L. Geng, Y.-K. Fang, and L.-Y. Peng, Robust segmented entangling gates with pulse gradient and power optimization using a hypersurface-tangent method, Phys. Rev. A **107**, 042617 (2023).

[43] A. E. Webb, S. C. Webster, S. Collingbourne, D. Bretaud, A. M. Lawrence, S. Weidt, F. Mintert, and W. K. Hensinger, Resilient Entangling Gates for Trapped Ions, Phys. Rev. Lett. **121**, 180501 (2018).

[44] R. Blümel, N. Grzesiak, N. Pisenti, K. Wright, and Y. Nam, Power-optimal, stabilized entangling gate between trapped-ion qubits, npj Quantum Inf. **7**, 147 (2021).

[45] M. Kang, Q. Liang, B. Zhang, S. Huang, Y. Wang, C. Fang, J. Kim, and K. R. Brown, Batch optimization of frequency-modulated pulses for robust two-qubit gates in ion chains, Phys. Rev. Appl. **16**, 024039 (2021).

[46] M. Li, M. Gutiérrez, S. E. David, A. Hernandez, and K. R. Brown, Fault tolerance with bare ancillary qubits for a [[7,1,3]] code, Phys. Rev. A **96**, 032341 (2017).

[47] M. A. Nielsen, A simple formula for the average gate fidelity of a quantum dynamical operation, Phys. Lett. A **303**, 249 (2002).

[48] T. Jones, A. Brown, I. Bush, and S. C. Benjamin, Quest and high performance simulation of quantum computers, Sci. Rep. **9**, 10736 (2019).

[49] S. Aaronson and D. Gottesman, Improved simulation of stabilizer circuits, Phys. Rev. A **70**, 052328 (2004).

[50] M. R. Geller and Z. Zhou, Efficient error models for fault-tolerant architectures and the Pauli twirling approximation, Phys. Rev. A **88**, 012314 (2013).

[51] M. Gutiérrez, C. Smith, L. Lulushi, S. Janardan, and K. R. Brown, Errors and pseudothresholds for incoherent and coherent noise, Phys. Rev. A **94**, 042338 (2016).

[52] M. Gutiérrez, M. Müller, and A. Bermúdez, Transversality and lattice surgery: Exploring realistic routes toward coupled logical qubits with trapped-ion quantum processors, Phys. Rev. A **99**, 022330 (2019).

[53] C. R. Clark, H. N. Tinkey, B. C. Sawyer, A. M. Meier, K. A. Burkhardt, C. M. Seck, C. M. Shappert, H. T. Hayden, W. G. Rellergert, K. R. Brown, *et al.*, High-Fidelity Bell-State Preparation with $^{40}Ca^+$ Optical Qubits, Phys. Rev. Lett. **127**, 130505 (2021).

[54] S. D. Fallek, C. D. Herold, B. J. McMahon, K. M. Maller, K. R. Brown, and J. M. Amini, Transport implementation

of the Bernstein–Vazirani algorithm with ion qubits, New J. Phys. **18,** 083030 (2016).

[55] C. Ryan-Anderson, PECOS: Performance estimator of codes on surfaces (2019), https://github.com/PECOS-packages/PECOS.

[56] C. Ryan-Anderson, *Quantum algorithms, architecture, and error correction*, Ph.D. thesis, The University of New Mexico, 2018, https://digitalrepository.unm.edu/phyc_etds/203/.

[57] S. C. Doret, J. M. Amini, K. Wright, C. Volin, T. Killian, A. Ozakin, D. Denison, H. Hayden, C.-S. Pai, R. E. Slusher, and A. W. Harter, Controlling trapping potentials and stray electric fields in a microfabricated ion trap through design and compensation, New J. Phys. **14,** 073012 (2012).

[58] S. Fishman, G. De Chiara, T. Calarco, and G. Morigi, Structural phase transitions in low-dimensional ion crystals, Phys. Rev. B **77,** 064111 (2008).

[59] Z. Ni, S. Li, X. Deng, Y. Cai, L. Zhang, W. Wang, Z.-B. Yang, H. Yu, Y. Xu, D. Yu, *et al.*, Beating the break-even point with a discrete-variable-encoded logical qubit, Nature **616,** 56 (2023).

[60] J. P. Gaebler, T. R. Tan, Y. Lin, Y. Wan, R. Bowler, A. C. Keith, S. Glancy, K. Coakley, and D. J. Wineland, High-Fidelity Universal Gate Set for $^9Be^+$ Ion Qubits, Phys. Rev. Lett. **117,** 060505 (2016).

[61] P. Parrado-Rodríguez, C. Ryan-Anderson, A. Bermudez, and M. Müller, Crosstalk suppression for fault-tolerant quantum error correction with trapped ions, Quantum **5,** 487 (2021).